

Quantum erasers and probing classifications of entanglement via nuclear magnetic resonance

G. Teklemariam,¹ E. M. Fortunato,² M. A. Pravia,² Y. Sharf,² T. F. Havel,² D. G. Cory,^{2,*} A. Bhattaharyya,³ and J. Hou³

¹*Department of Physics, MIT, Cambridge, Massachusetts 02139*

²*Department of Nuclear Engineering, MIT, Cambridge, Massachusetts 02139*

³*Center for Excellence in Education, 140 Park Street SE, Vienna, Virginia 22180*

(Received 25 December 2001; published 24 July 2002)

We report the implementation of two- and three-spin quantum erasers using nuclear magnetic resonance (NMR). Quantum erasers provide a means of manipulating quantum entanglement, an important resource for quantum information processing. Here, we first use a two-spin system to illustrate the essential features of quantum erasers. The extension to a three-spin “disentanglement eraser” shows that entanglement in a subensemble can be recovered if a proper measurement of the ancillary system is carried out. Finally, we use the same pair of orthogonal decoherent operations used in quantum erasers to probe the two classes of entanglement in tripartite quantum systems: the Greenberger-Horne-Zeilinger state and the W state. A detailed presentation is given of the experimental decoherent control methods that emulate the loss of phase information in strong measurements, and the use of NMR decoupling techniques to implement partial trace operations.

DOI: 10.1103/PhysRevA.66.012309

PACS number(s): 03.67.-a, 03.65.-w

I. INTRODUCTION

The term “quantum eraser” [1] was invented to describe the loss or gain of interference or, more generally quantum information, in a subensemble, based on the measurement outcomes of two complementary observables. Recently, the quantum eraser was extended to three qubits, thus enabling quantum information stored in a pair of qubits mutually entangled with a third to be manipulated. This was dubbed the “quantum disentanglement eraser” [2], and has been demonstrated by us using nuclear magnetic resonance (NMR) techniques [3].

In many quantum information processing (QIP) applications, entanglement is central to the transfer and sharing of information. While two-particle entanglement is well classified, for three or more particles the situation is more complex. For example, while there are two classes of entanglement for three particles [4], there are nine types of entanglement for four particles [5]. Consequently, there has been a significant effort directed at quantifying these different types of entanglement and many metrics have been proposed [6–10]. In particular, a classification strategy, based on local operations assisted by classical communication (LOCC) [4], has been established.

Here, we extend our earlier work on an NMR analog of the quantum disentanglement eraser to the study two- and three-spin quantum erasers, and use complementary measurements (i.e., a pair of orthogonal measurements), as a probe of entanglement classes in the case of three qubits. Previously, the quantum disentanglement eraser was demonstrated on a GHZ state. We contrast this with complementary measurements applied to the W state, which differs from the GHZ state in the entanglement destroyed upon tracing over any single qubit. Furthermore, we give an expanded treatment of the experimental details of an NMR implementation of quantum erasers beyond that presented in Ref. [3].

II. SOME PROPERTIES OF TRIPARTITE ENTANGLEMENT

Entanglement, which has been related to the nonlocal properties of a quantum state, is a characteristic feature of quantum systems. Presently, QIP research is revealing that multipartite states can be entangled in different ways. For instance, there are two classes of entanglement for three-qubit systems [4]: one represented by the GHZ state

$$|\text{GHZ}\rangle = \frac{1}{\sqrt{2}}(|000\rangle + |111\rangle), \quad (1)$$

and another by the W state

$$|W\rangle = \frac{1}{\sqrt{3}}(|001\rangle + |010\rangle + |100\rangle). \quad (2)$$

These two classes are inequivalent because states from one cannot be obtained from states of the other by single-particle (i.e., local) operations. Another key difference is that a single-particle trace of the GHZ state results in a maximally mixed state compared with a nonmaximally mixed result for the W state.

Many different metrics have been proposed to quantify the “amount” of entanglement each state contains; each metric emphasizing a specific feature or property of multiparticle entanglement. Amongst the many proposed multiparticle entanglement metrics such as the concurrence [6], the n tangle [7], the Schmidt rank [8], the negativity [9], etc., the one proposed by Meyer *et al.* in Ref. [10] is most relevant to the present work because we are interested in the entanglement properties of a subsystem following local decoherent operations on a portion of a composite system. For a given state ψ , the metric of Meyer *et al.* is an average over each qubit subsequent to “tracing” over each binary state and comparing how orthogonal the remaining states are. It is defined as

*Email address: dcory@mit.edu

$$Q(\psi) = \frac{4}{n} \sum_{j=1}^n D(\iota_j(0)\psi, \iota_j(1)\psi), \quad (3)$$

where n is the number of qubits and the operation ι defines the map

$$\iota_j(b)|b_1 \cdots b_n\rangle = \delta_{bb_j} |b_1 \cdots \hat{b}_j \cdots b_n\rangle \quad (4)$$

for $b \in \{0,1\}$ and the caret denotes absence. $D(u,v)$ is the norm squared of the wedge product between the states u and v , which measures how orthogonal they are. For example, $Q(|W\rangle) = 8/9$ and $Q(|\text{GHZ}\rangle) = 1$ [for reference, $Q(|000\rangle) = 0$], which shows that the GHZ state is the maximally entangled three-qubit state.

Complementary measurements also reveal differences between the GHZ and W states. While a measurement of one qubit of the GHZ state along the z axis results in two separable subensembles, an orthogonal measurement (for instance, along the x axis) results in maximally entangled subensembles. Alternatively, the same set of measurements applied to the W state does not result in such a stark difference in the states of the unmeasured qubits.

III. QUANTUM ERASERS

A. Two-particle quantum eraser

Two-particle quantum erasers have been extensively discussed in the literature [1,11–13]. The basic idea is that measurement of one qubit in a Bell state leads to collapse of the second; therefore the viability of information, in an entangled state, depends on what actions are carried out on the second qubit. For example, consider a qubit A in the superposition state

$$|+\rangle_A = \frac{1}{\sqrt{2}}(|0\rangle_A + |1\rangle_A). \quad (5)$$

Qubit A is then entangled with another qubit B , which plays the role of an ancilla qubit creating the Bell state

$$|\Psi_{AB}\rangle = \frac{1}{\sqrt{2}}(|0\rangle_A|0\rangle_B + |1\rangle_A|1\rangle_B). \quad (6)$$

The reduced density matrix of qubit A , obtained by tracing over qubit B in $|\Psi_{AB}\rangle$, would reveal that qubit A is no longer in a superposition state. The key idea in the eraser scheme is the manipulation of the state of qubit A by operations on qubit B alone. Thus, measurements on qubit B along the quantization axis will collapse qubit A to an eigenstate, while measurements on qubit B along an orthogonal axis to the quantization axis will restore the coherence of qubit A . This effect is called a “quantum eraser” because the restoration of qubit A ’s coherence was the result of “erasing” the information stored in qubit B , in the joint state $|\Psi_{AB}\rangle$, by measuring qubit B along a direction orthogonal to the quantization axis. The quantum eraser demonstrates the principle of complementarity without invoking the corresponding uncertainty principle, because the measurements on qubit B are based on

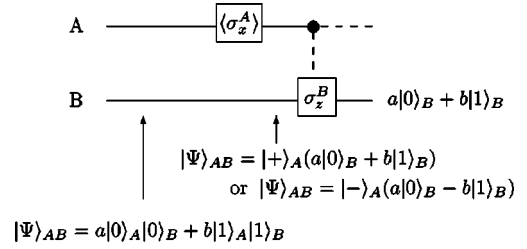


FIG. 1. Proposed QIP application for the quantum eraser. Two qubits, A and B , which are part of a quantum communication network are entangled with arbitrary complex coefficients a and b . This shared information can be transferred to either qubit by local operations if both qubits are accessible. If the qubits interact weakly or they are locally inaccessible, the information can still be transferred to either qubit by using the quantum-eraser scheme. If it is required that the data be transferred to qubit B , this can be accomplished by a σ_x^A measurement on qubit A projecting qubit B into the state $a|0\rangle_B \pm b|1\rangle_B$, where the sign depends on the measurement outcome of qubit A , $|+\rangle_A$, respectively. Furthermore, the state of qubit A subsequent to the measurement can be treated as an “error syndrome” to correct the relative sign of qubit A by communicating this information via a classical channel. Once the two qubits get entangled the network is symmetric between them and the data can be equivalently be transferred to qubit A by switching the operations between the two qubits.

two complementary observables whose outcome, probed by the state of qubit A , produce mutually exclusive results.

The quantum-eraser scheme may find applications in communications networks that require the transfer of information amongst qubits that interact weakly, or where one qubit may be locally inaccessible. Figure 1 shows a network for two qubits that may be part of some communications network. Because the network is symmetric for the two qubits the information can equally be transferred to qubit A by performing an orthogonal measurement on qubit B . Furthermore, similar to quantum teleportation and error correction schemes, the measurement outcomes on the decohered qubit can be treated as an error syndrome, and this information can be used to recover the relative phase between the states of the data qubit. This application clearly illustrates that the “quantum-eraser scheme” is an example of LOCC.

B. Three-particle quantum erasers

While two qubits are the minimum required for quantum erasers, three qubits provide the interesting possibility of manipulating entanglement among two of the qubits.

1. The GHZ state

In the disentanglement eraser the components of a GHZ state are regarded as the components of a two-qubit Bell state labeled by the state of a third ancilla qubit A , as follows:

$$|\psi_{\text{GHZ}}\rangle = \frac{1}{\sqrt{2}}(|0_A\rangle|00\rangle + |1_A\rangle|11\rangle). \quad (7)$$

A projective measurement of the ancilla in this basis yields a pair of separable states $|00\rangle$ and $|11\rangle$ labeled by the ancilla qubit, realizing the ensemble

$$E_+^A|00\rangle\langle 00| + E_-^A|11\rangle\langle 11|. \quad (8)$$

Alternatively, if the ancilla is measured along the x axis a pair of complementary Bell states, $|\phi_{\pm}\rangle = 1/\sqrt{2}(|00\rangle \pm |11\rangle)$, labeled by the ancilla is obtained. To see this we rewrite the GHZ state in a basis with the ancilla qubit quantized along the x axis

$$\begin{aligned} |\psi_{\text{GHZ}}\rangle &= 1/\sqrt{2}[1/\sqrt{2}(|+_A\rangle + |-_A\rangle)|00\rangle \\ &\quad + 1/\sqrt{2}(|+_A\rangle - |-_A\rangle)|11\rangle] \\ &\equiv 1/\sqrt{2}(|+_A\rangle|\phi_+\rangle + |-_A\rangle|\phi_-\rangle). \end{aligned} \quad (9)$$

A measurement of the ancilla along the x axis, followed by a rotation of the ancilla to the z axis thus results in the ensemble

$$E_+^A|\phi_+\rangle\langle\phi_+| + E_-^A|\phi_-\rangle\langle\phi_-|, \quad (10)$$

which is a mixture of complementary Bell states each labeled by the state of the ancilla. Thus, measurements of the ancilla qubit along the x axis realizes a pair of subensembles of entangled states.

2. The W state

Like the GHZ state of the disentanglement eraser, the components of a W state can be regarded as the Bell states $|\psi_{\pm}\rangle = 1/\sqrt{2}(|01\rangle \pm |10\rangle)$ together with the classical state $|00\rangle$, labeled by the state of a third ancilla qubit (given the subscript “ A ”), as follows:

$$|W\rangle = \frac{1}{\sqrt{3}}[|0_A\rangle(|01\rangle + |10\rangle) + |1_A\rangle|00\rangle]. \quad (11)$$

A measurement of the ancilla qubit along the z axis yields the ensemble

$$E_+^A|\tilde{\psi}_+\rangle\langle\tilde{\psi}_+| + E_-^A|00\rangle\langle 00|, \quad (12)$$

where $|\tilde{\psi}_+\rangle = \sqrt{2}|\psi_+\rangle$. Rewriting the W state with the ancilla qubit represented along the x axis yields

$$\begin{aligned} |W\rangle &= \frac{1}{\sqrt{3}}[1/\sqrt{2}(|+_A\rangle + |-_A\rangle)|\tilde{\psi}_+\rangle \\ &\quad + 1/\sqrt{2}(|+_A\rangle - |-_A\rangle)|00\rangle] \\ &\equiv 1/\sqrt{2}[|+_A\rangle(|\tilde{\psi}_+\rangle + |00\rangle) + |-_A\rangle(|\tilde{\psi}_+\rangle - |00\rangle)]. \end{aligned} \quad (13)$$

Therefore, a measurement of the ancilla qubit along the x axis then followed by a rotation of the ancilla back to the z axis results in the ensemble

$$\begin{aligned} &E_+^A(|\tilde{\psi}_+\rangle\langle\tilde{\psi}_+| + |\tilde{\psi}_+\rangle\langle 00| + |00\rangle\langle\tilde{\psi}_+| + |00\rangle\langle 00|) \\ &+ E_-^A(|\tilde{\psi}_+\rangle\langle\tilde{\psi}_+| - |\tilde{\psi}_+\rangle\langle 00| - |00\rangle\langle\tilde{\psi}_+| - |00\rangle\langle 00|) \\ &\times \langle\tilde{\psi}_+| + |00\rangle\langle 00|, \end{aligned} \quad (14)$$

which is a mixture of a Bell state plus a classical state and products of these states. Thus, the W state still retains entanglement even under a z -axis measurement of the ancilla qubit.

IV. NMR CONTROL METHODS

The recent development of precise coherent [14] and de-coherent [15] control methods makes liquid-state NMR a particularly good test bed for exploring quantum erasers. Liquid-state NMR implementations of QIP typically rely on chemically distinct spin- $\frac{1}{2}$ nuclei for qubits [16]. In a liquid NMR sample, the correlations between the spin states of nuclei in different molecules is averaged to zero by molecular motion, and hence we only focus on the intramolecular correlations. For sensitivity purposes an ensemble of $\sim 10^{18}$ molecules is typically used. Therefore, a liquid-state NMR QIP has $\sim 10^{18}$ quantum processors, and a density matrix is needed to describe the statistics of measurements on this system.

When the spins are in thermal equilibrium their density matrix is given by the Boltzmann operator. In the high-temperature approximation this is given by

$$\rho_{\text{eq}} \approx I + \frac{1}{2}\beta \sum_{i=1}^3 \gamma_i \sigma_z^i, \quad (15)$$

where $\beta\gamma_i \approx 10^{-5}$ at room temperatures [17], γ_i is the gyro-magnetic ratio of each nucleus, and σ_z is one of the Pauli matrices $\{I, \sigma_x, \sigma_y, \sigma_z\}$, (I is the identity matrix). The density matrices of these systems is highly mixed, but can be transformed into a pseudopure state [18] having the form

$$\rho = \frac{(1-\epsilon)}{2^N} I + \epsilon |\psi\rangle\langle\psi|, \quad (16)$$

where $\epsilon = \beta N/2^N$ and N is the number of spins. Under unitary transformations $\rho' = \mathcal{U}\rho\mathcal{U}^{-1}$, the identity part transforms trivially while the underlying state vector $|\psi\rangle$ transforms one-sidedly to $\mathcal{U}|\psi\rangle$, exactly as it would for a true pure state.

In NMR, the signal detected is a *spatial* ensemble average given by the trace of the product of the transverse magnetic-field components with the density matrix:

$$\langle M_x(t) + iM_y(t) \rangle = \gamma \text{Tr}\{(\sigma_x + i\sigma_y)\rho(t)\}, \quad (17)$$

where $\rho(t) = \mathcal{U}_{\text{int}}\rho(t_0)\mathcal{U}_{\text{int}}^{-1}$, $\mathcal{U}_{\text{int}} = e^{-i\mathcal{H}_{\text{int}}t}$, \mathcal{H}_{int} is the internal Hamiltonian of the spins, and $\rho(t_0)$ is the state of the spin system right before detection starts. Alternatively, a partial trace operation can be implemented by NMR decoupling techniques. These techniques are normally used to simplify spectra of multiple spins, by removing the splittings caused by the decoupled spin. The z component of the spin to be decoupled is rapidly modulated with respect to the time scale of the inverse coupling constant. This ensures that the decoupled spin has no effect upon the measurements and so implements a partial trace operation.

The effect of decoupling on the density matrix can be seen by first writing the density matrix of the spin system in terms of the subspaces of spin i , or the single element operators of spin i

$$\rho = \begin{bmatrix} |0\rangle_i \langle 0| \otimes \rho_{1\ldots\hat{i}\ldots N}^{11} & |0\rangle_i \langle 1| \otimes \rho_{1\ldots\hat{i}\ldots N}^{12} \\ |1\rangle_i \langle 0| \otimes \rho_{1\ldots\hat{i}\ldots N}^{21} & |1\rangle_i \langle 1| \otimes \rho_{1\ldots\hat{i}\ldots N}^{22} \end{bmatrix}, \quad (18)$$

where \hat{i} indicates the absence of spin i . The subspaces of spin i can also be represented by the transition operators that are written here in terms of the geometric algebra (GA) notation [19]:

$$|0\rangle_i \langle 0| = E_+^i = \frac{1}{2}(I + \sigma_z^i), \quad (19)$$

$$|0\rangle_i \langle 1| = E_+^i \sigma_x^i = \frac{1}{2}(I + \sigma_z^i) \sigma_x^i, \quad (20)$$

$$|1\rangle_i \langle 0| = \sigma_x^i E_+^i = \sigma_x^i \frac{1}{2}(I + \sigma_z^i), \quad (21)$$

$$|1\rangle_i \langle 1| = E_-^i = \frac{1}{2}(I - \sigma_z^i). \quad (22)$$

Decoupling renders σ_x^i and σ_z^i unobservable thus reducing E_{\pm}^i to the identity term I . The density matrix then becomes

$$\rho_r = \rho_{1\ldots\hat{i}\ldots N}^{11} + \rho_{1\ldots\hat{i}\ldots N}^{22}, \quad (23)$$

and the effective Hilbert space is reduced to that of the undecoupled spins. This may be compared with the mathematical definition of the partial trace over qubit i :

$$\begin{aligned} \text{Tr}\{\rho\} &= \sum_k \langle k| \rho |k\rangle_i = \langle 0| \rho |0\rangle_i + \langle 1| \rho |1\rangle_i = \rho_{1\ldots\hat{i}\ldots N}^{11} \\ &+ \rho_{1\ldots\hat{i}\ldots N}^{22}. \end{aligned} \quad (24)$$

The implementation by NMR techniques proceeds as follows. Consider N spins whose interaction Hamiltonian, in the weak-coupling limit, is [17]

$$\mathcal{H}_{\text{int}} = \sum_{k=1}^N \nu_k \sigma_z^k + \sum_{j>k}^N \sum_{k=1}^N J_{kj} \sigma_z^k \sigma_z^j, \quad (25)$$

where ν is a chemical shift constant while J is a coupling constant. This system will exhibit $N2^{N-1}$ spectral lines (corresponding to transitions between energy levels). To remove the splittings, decoupling techniques are used to selectively “turn off” the interaction between the spins. This decoupling Hamiltonian [20] takes the form

$$\mathcal{H}_{\text{dec}} \propto \nu_{\text{RF}} \sigma_x^i, \quad (26)$$

where $\nu_{\text{RF}} \gg J_{ij}$ for all j . \mathcal{H}_{dec} is applied continuously during the signal observation period. Consequently, spin i will nutate about the x axis, and all terms of the density matrix involving spin i , such as σ_x^i , $\sigma_z^1 \sigma_x^i$, $\sigma_x^1 \sigma_z^2 \cdots \sigma_z^i \cdots \sigma_z^N$, etc., will be rendered unobservable. More generally, the internal Hamiltonian is transformed to

$$\tilde{\mathcal{H}}_{\text{int}} = \mathcal{U}_{\text{dec}} \mathcal{H}_{\text{int}} \mathcal{U}_{\text{dec}}^{-1} = \sum_{\substack{k=1 \\ \{k \neq i\}}}^N \nu_k \sigma_z^k + \sum_{j>k}^N \sum_{\substack{k=1 \\ (k \neq i)}}^N J_{kj} \sigma_z^k \sigma_z^j. \quad (27)$$

Therefore, measurements of the spin system during this period yields no information about spin i , implementing the partial trace over the decoupled spin.

Another experimental means of implementing nonunitary operations is the use of linear magnetic-field gradients. By taking advantage of the spatial extent of an NMR sample, a magnetic-field gradient, $\nabla = \partial B_z / \partial z$, applied parallel to the static field direction, causes the spins’ Larmor precession frequency to vary linearly with their spatial coordinates. This results in evolution under the Hamiltonian

$$\mathcal{H}_{\text{grad}} = \gamma \nabla z \frac{1}{2} \sum_j \sigma_z^j, \quad (28)$$

according to the Liouville von Neumann equation

$$i\hbar \frac{\partial \rho}{\partial t} = [\rho, \mathcal{H}]. \quad (29)$$

Subsequently, each coherence $\rho_{k\ell}$ ($k \neq \ell$) is multiplied by a spatially dependent phase $\exp(-i\gamma m_{k\ell} \nabla z t / 2)$, where $m_{k\ell}$ is the *coherence order* [15,17,21] (i.e., the difference in the z component of the angular momentum between the $|k\rangle$ and $|\ell\rangle$ states in units of \hbar). After such a gradient pulse the density matrix, averaged over the sample volume, results in an incoherent sum, and satisfies $\rho_{k\ell} = 0$ for all $k \neq \ell$ except for the zero quantum coherences ($m_{k\ell} = 0$). This spatially dependent phase is reversible provided the spins have not changed location. If diffusion is allowed to take place, this incoherent evolution is rendered decoherent because the motion of the spins destroys the correlation between the phase and location.

In this study, linear magnetic-field gradients were used to dephase the coherences of ρ , to wipe out magnetization during the experiments, and as also happens in strong measurements of σ_z [22]. This dephasing operation was made spin specific by applying a series of π pulses to the other spins, interleaved by gradient pulses of the same amplitude and duration, to “refocus” all the other coherences and at the same time also refocus the evolution under the internal Hamiltonian. Such refocusing schemes are well known in NMR [17] and apply here by recognizing that evolution under \mathcal{H} is similar to evolution under a chemical shift interaction term. In particular, a refocusing scheme that scales polynomially, in the number of time periods and π pulses as the number of spins grows, has been proposed in Ref. [23].

To “measure” along any axis (j), the spins frame is rotated such that j is now along z . Then, the spins are subjected to a selective evolution under \mathcal{H} . Finally, the frame is rotated back by the inverse of the rotation that took the spins from j to z .

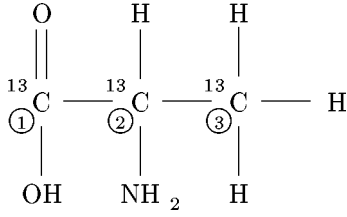


FIG. 2. The alanine molecule. The encircled labels on the ^{13}C s index the spins used in the experiment.

V. EXPERIMENTAL DEMONSTRATIONS

The quantum erasers in this presentation were demonstrated on ensembles of molecules, each containing two spin- $\frac{1}{2}$ nuclei for the two-particle quantum-eraser effect and three spin- $\frac{1}{2}$ nuclei for all the three-particle quantum-eraser effects. All experiments were performed using standard Bruker spectrometers. The two-spin experiments were performed on the two-spin heteronuclear spin system ^{13}C -labeled chloroform ($^{13}\text{CHCl}_3$) diluted with deuterated acetone. The two spins used were the ^{13}C and H nucleus and they exhibited a weakly coupled spectrum corresponding to the internal Hamiltonian

$$\mathcal{H}_{\text{int}} = \pi \left[\nu_{\text{C}} \sigma_z^{\text{C}} + \nu_{\text{H}} \sigma_z^{\text{H}} + \frac{J}{2} \sigma_z^{\text{C}} \sigma_z^{\text{H}} \right], \quad (30)$$

where the ν 's are Larmor frequencies ($\nu_{\text{H}}/\nu_{\text{C}} \approx 4$) and J the spin-spin coupling constant in Hertz. Due to the huge difference in the chemical shifts between ^{13}C and H we use two channels thereby placing each nuclei in a corotating frame with no net Zeeman evolution. Thus, ν_{H} and ν_{C} were set to zero in the respective frames of each nuclei, and $J = 214$ Hz.

The three-spin experiments used the three spin- $\frac{1}{2}$ carbons in a ^{13}C -labeled sample of alanine in deuterated water (Fig. 2). With decoupling of the protons [17], this spin system exhibits a weakly coupled spectrum corresponding to the Hamiltonian

$$\mathcal{H}_{\text{int}} = \pi [\nu_1 \sigma_z^1 + \nu_2 \sigma_z^2 + \nu_3 \sigma_z^3 + \frac{1}{2} (J_{12} \sigma_z^1 \sigma_z^2 + J_{23} \sigma_z^2 \sigma_z^3 + J_{13} \sigma_z^1 \sigma_z^3)], \quad (31)$$

where the ν 's are Larmor frequencies and the J 's the spin-spin coupling constants in Hertz. The frequency shifts of the carbon resonances with respect to the second are 9456.5 Hz (31.5216 ppm) for the first one and -2594.3 Hz (8.6476 ppm) for the third, while the coupling constants are $J_{12} = 53.7$, $J_{23} = 34.6$, and $J_{13} = -1.4$ Hz. The T_1 relaxation times for the three spins are 21, 2.5, and 1.6 s, while the T_2 times are 550, 420, and 800 ms, respectively.

In the two-spin case the equilibrium density matrix is given in the high-temperature approximation by

$$\rho_{\text{eq}} \approx I + \beta \left(\sigma_z^{\text{C}} + \frac{\gamma_{\text{H}}}{\gamma_{\text{C}}} \sigma_z^{\text{H}} \right), \quad (32)$$

where the ratio of the gyromagnetic ratio is $\gamma^{\text{H}}/\gamma^{\text{C}} \approx 4$. By the procedure described in Ref. [24] ρ_{eq} is transformed to

TABLE I. This table shows the transformations used to obtain the three-spin pseudopure state from the thermal equilibrium state, using geometric algebra notation [19,25].

Transformations	
(1)	$ \nabla e^{-(1/2) \cos^{-1}(\sqrt{3}/4\sqrt{2}) \sigma_z^2}$
(2)	$ \nabla e^{-i(\pi/4)(\sigma_y^1 + \sigma_y^3) E_-^2}$
(3)	$e^{i(\pi/4) \sigma_x^1} e^{-i(\pi/4) \sigma_z^1 \sigma_z^2} e^{-i(\pi/4)(\sigma_y^1 + \sigma_y^3)} e^{-i(\pi/4) \sigma_z^1 \sigma_z^2} e^{-i(\pi/4) \sigma_z^1 \sigma_z^2}$
(4)	$ \nabla e^{i(\pi/12)(\sigma_y^2 + \sigma_y^3)} e^{-i(\pi/4) \sigma_z^1 \sigma_z^2} e^{-i(\pi/8)(\sigma_x^2 + \sigma_x^3)}$

$$\rho = I + \beta \left(1 + \frac{\gamma_{\text{H}}}{\gamma_{\text{C}}} \right) (\sigma_z^{\text{C}} + \sigma_z^{\text{H}}), \quad (33)$$

which has a balanced spin population compared to the equilibrium state. Because ρ has a different eigenvalue structure relative to ρ_{eq} a nonunitary operation was required, i.e., a gradient pulse, as part of the sequence of transformations. To transform ρ to the desired pseudopure (PP) state, we use the two-spin pseudopure state preparation sequence described in Ref. [25], which yields

$$\rho_{\text{PP}} = \frac{1}{4} (I + \sigma_z^{\text{C}} + \sigma_z^{\text{H}} + \sigma_z^{\text{C}} \sigma_z^{\text{H}}) \quad (34)$$

ignoring nonessential constants. We also designate $\hat{\rho}_{\text{ini}} = \rho_{\text{PP}} - \frac{1}{4} I$ as the traceless part of the initial state used in the experiment.

For the three-spin case, the pseudopure ground state was prepared from the thermal equilibrium state by the procedure summarized in Table I, which uses magnetic-field gradients (denoted by $|\nabla|$) to dephase off-diagonal elements of the density matrix along the way [18] just as in the two-spin case. Letting $\hat{\rho}_{\text{eq}} = \sigma_z^1 + \sigma_z^2 + \sigma_z^3$ be the traceless part of the equilibrium density matrix (which has a balanced spin population to start with and with all physical constants set to unity), the first two transformations in the table yield the state $(\sqrt{3}/\sqrt{32}) \sigma_z^2 + (\sigma_z^1 + \sigma_z^3) E_+^2$. The third transformation in Table I swaps spins 1 and 2 yielding $(\sqrt{3}/\sqrt{32}) \sigma_z^1 + (\sigma_z^2 + \sigma_z^3) E_+^1$. Spins 2 and 3 may then be transformed into the state $(\sqrt{3}/\sqrt{32}) (\sigma_z^2 + \sigma_z^3 + \sigma_z^2 \sigma_z^3)$ by the two-spin pseudopure state preparation procedure used in Eq. (34), yielding the three-spin pseudopure ground state

$$\hat{\rho}_{\text{ini}} = \frac{\sqrt{3}}{\sqrt{32}} (E_+^1 E_+^2 E_+^3 - \frac{1}{8} I) \equiv (|000\rangle\langle 000| - \frac{1}{8} I). \quad (35)$$

A. The two-spin quantum eraser

The two-spin quantum eraser was implemented according to the logic network shown in Fig. 3. A superposition state is first created on spin 2 and then correlated to the ancillary spin to create $\hat{\rho}_{\text{Bell}}$. The coherences of $\hat{\rho}_{\text{Bell}}$ can be selectively dephased as described above with the pulse sequence,

$$P_z^1 = [|\nabla|_z - [\pi]_x^2 - [|\nabla|_z - [\pi]_{-x}^2]. \quad (36)$$

To dephase spin 1 in the same way as would a strong measurement of σ_x^1 , we apply the pulse sequence

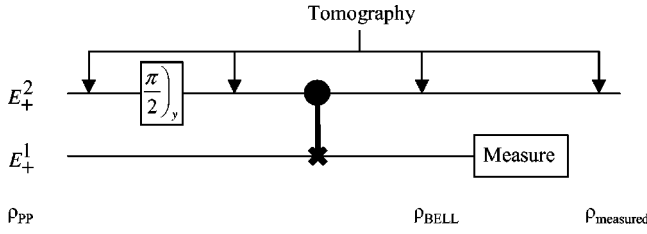


FIG. 3. Logic network for the two-spin quantum eraser. Initially, a pseudopure state on spins 1 and 2 is created, $\rho_{PP} = |00\rangle\langle 00| \equiv E_+^1 E_+^2$. A $\pi/2$ y pulse is then applied to spin 2, followed by a controlled-NOT (c-NOT) gate [26] to create the Bell state (see text). Conditionally on the second spin being in the $|1\rangle$ state is represented in the network by a filled circle on its time line. Finally, one of the two complementary measurements, σ_z^1 or σ_x^1 , are applied to spin 1. State tomography was performed to fully reconstruct the density matrices at the positions indicated.

$$P_x^1 = [\pi/2]_{-y}^1 - P_z^1. \quad (37)$$

Spin 1 is left along z for subsequent tomography [27].

The results of P_z^1 and P_x^1 applied to $\hat{\rho}_{Bell}$ are

$$\hat{\rho}_{Bell} \xrightarrow{P_z^1} \frac{1}{2}(E_+^1 E_+^2 + E_-^1 E_-^2 - \frac{1}{2}I), \quad (38)$$

$$\hat{\rho}_{Bell} \xrightarrow{P_x^1} \frac{1}{2}[(1 + \sigma_x^2)E_+^1 + (1 - \sigma_x^2)E_-^1 - \frac{1}{2}I], \quad (39)$$

where $\frac{1}{2}(1 \pm \sigma_x) = |\pm\rangle\langle \pm|$. Tomography was performed at the points of the procedure indicated in Fig. 3; the real parts of these four density matrices are shown in Fig. 4 (the imaginary parts were essentially zero).

The overall precision of quantum information transmission was quantified by the *attenuated correlation* [3,14]. It takes into account not only systematic errors, but also the net loss of magnetization due to random errors. The values of the correlation for each of the four tomographic readouts were $c(\hat{\rho}_{PP}^{ext})=1$ (by definition), $c(\hat{\rho}_{Bell}^{ext})=0.98$, $c(\hat{\rho}_z^{ext})=0.97$, and $c(\hat{\rho}_x^{ext})=0.98$. The increases in c are not unexpected, since the additional π and gradient pulses needed to mimic measurements on $\hat{\rho}_{Bell}$ are easily implemented with high precision, and the tomographic errors are estimated at $\pm 1\%$. Thus, clearly the σ_x^1 measurement on $\hat{\rho}_{Bell}$ restores the coherence of spin 2 in the two subensembles distinguished by the state of spin 1.

B. Three-particle quantum erasers

1. The GHZ state

The logic network shown in Fig. 5 transforms the initial pseudopure state into the pseudopure GHZ state, and then decoheres the ancilla as indicated. The GHZ state is obtained by rotating spin 2 (since $J_{13} \ll J_{12}, J_{23}$) to the x axis and then using it as the control for a pair of controlled-NOT (c-NOT) gates to the other spins (see [3]). The resulting pseudopure GHZ state is written in GA notation as [19]

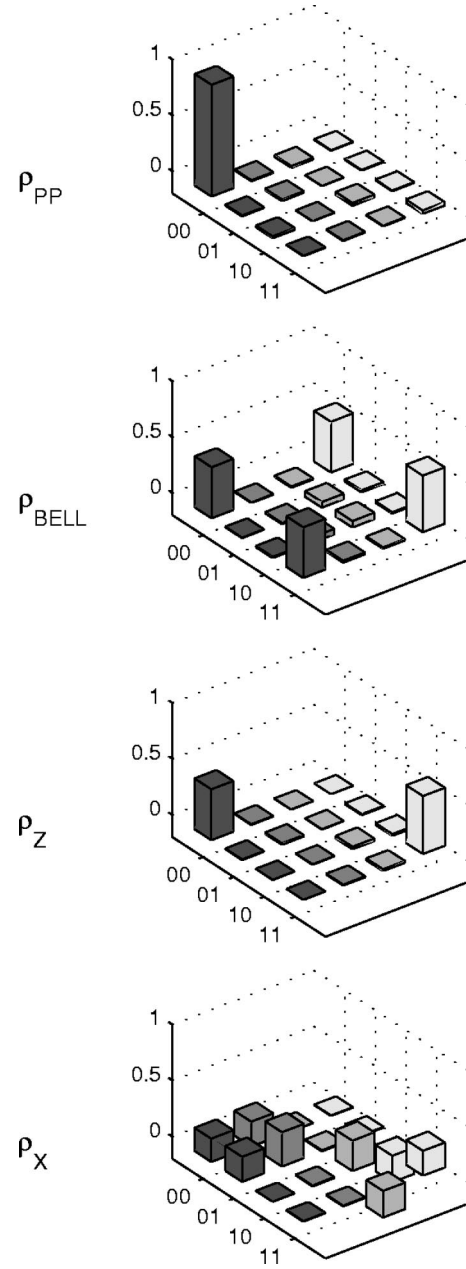


FIG. 4. Experimental density matrices reconstructed by tomography (in normalized units). The rows are enumerated in the standard computational basis, where, for example, 00 represents the state label $|00\rangle$. Although not shown, the columns are similarly labeled with the leftmost end representing $|00\rangle$ and the rightmost end representing $|11\rangle$. ρ_{PP} is the three-spin pseudopure ground state, and ρ_{Bell} is the pseudopure Bell state. The last two plots are ρ_z , which is ρ_{Bell} after decohering spin 1 about the z axis, and ρ_x , which is after decohering it about the x axis. An amount of identity, chosen to optimize the input projection, was added to all experimentally measured density matrices.

$$\begin{aligned} \hat{\rho}_{GHZ} = & \frac{\sqrt{3}}{4\sqrt{2}} \left[\frac{1}{2} E_+^1 (E_+^2 E_+^3) + \frac{1}{2} E_-^1 (E_-^2 E_-^3) \right. \\ & + \frac{1}{2} \sigma_x^1 E_+^1 (\sigma_x^2 E_+^2 \sigma_x^3 E_+^3) \\ & \left. + \frac{1}{2} \sigma_x^1 E_-^1 (\sigma_x^2 E_-^2 \sigma_x^3 E_-^3) - \frac{1}{8} I \right]. \end{aligned} \quad (40)$$

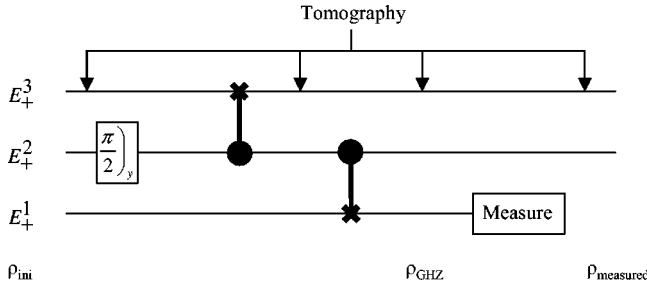


FIG. 5. Logic network for the disentanglement eraser. Initially, a pseudopure state on spins 1, 2, and 3 is created, $\rho_{\text{ini}} = |000\rangle\langle 000| \equiv E_+^1 E_+^2 E_+^3$. A $\pi/2$ y pulse is then applied to spin 2, followed by two controlled-NOT (c-NOT) gates [26] to create the GHZ state (see text). Conditionality on the second spin being in the $|1\rangle$ state is represented in the network by a filled circle on its time line. Finally, the two complementary measurements, σ_z^1 and σ_x^1 , are applied to spin 1. State tomography was performed to fully reconstruct the density matrices at the positions indicated.

The notation expresses $\hat{\rho}_{\text{GHZ}}$ in terms of the state of spin 1, and also shows the symmetry of the state under particle exchange. This state has previously been studied by NMR in Ref. [28].

The coherences of $\tilde{\rho}_{\text{GHZ}}$ can be dephased as described above with the following sequence of RF and gradient pulses:

$$P_z^1 = [\nabla]_z - [\pi]_x^2 - [\nabla]_z - [\pi]_x^{2,3} - [\nabla]_z - [\pi]_{-x}^2 - [\nabla]_z - [\pi]_{-x}^{2,3}. \quad (41)$$

The following pulse sequence dephases the ancilla in the same way as would a strong measurement of σ_x^1 :

$$P_x^1 = [\pi/2]_{-y}^1 - P_z^1. \quad (42)$$

For subsequent tomography the ancilla is left along z.

The results of P_z^1 and P_x^1 applied to $\hat{\rho}_{\text{GHZ}}$ are

$$\hat{\rho}_{\text{GHZ}} \xrightarrow{P_z^1} \frac{\sqrt{3}}{4\sqrt{2}} \left[\frac{1}{2} E_+^1 (E_+^2 E_+^3) + \frac{1}{2} E_-^1 (E_-^2 E_-^3) - \frac{1}{8} I \right], \quad (43)$$

$$\hat{\rho}_{\text{GHZ}} \xrightarrow{P_x^1} \frac{\sqrt{3}}{4\sqrt{2}} \left[\frac{1}{2} E_+^1 (1 + \sigma_x^2 \sigma_x^3) (E_+^2 E_+^3 + E_-^2 E_-^3) + \frac{1}{2} E_-^1 (1 - \sigma_x^2 \sigma_x^3) (E_+^2 E_+^3 + E_-^2 E_-^3) - \frac{1}{8} I \right]. \quad (44)$$

Thus, noting that the states $|\phi\pm\rangle\langle\phi\pm|$ have the GA representation $\frac{1}{2}(1 \pm \sigma_x^2 \sigma_x^3)(E_+^2 E_+^3 + E_-^2 E_-^3)$, the P_z^1 measurement realizes the ensemble in Eq. (8) while the P_x^1 measurement realizes the ensemble in Eq. (10). Tomography was performed at the points of the procedure indicated in Fig. 5; the real parts of these four density matrices are shown in Fig. 6 (the imaginary parts were again essentially zero).

The values of the attenuated correlation for each of the four tomographic readouts were $c(\hat{\rho}_{\text{ini}}^{\text{expt}}) = 1$ (by definition), $c(\hat{\rho}_{\text{GHZ}}^{\text{expt}}) = 0.88$, $c(\hat{\rho}_z^{\text{expt}}) = 0.92$, and $c(\hat{\rho}_x^{\text{expt}}) = 0.93$. Tomography on the intermediate state $|0\rangle\langle 00| + |11\rangle\langle 11|/\sqrt{2}$ yields an

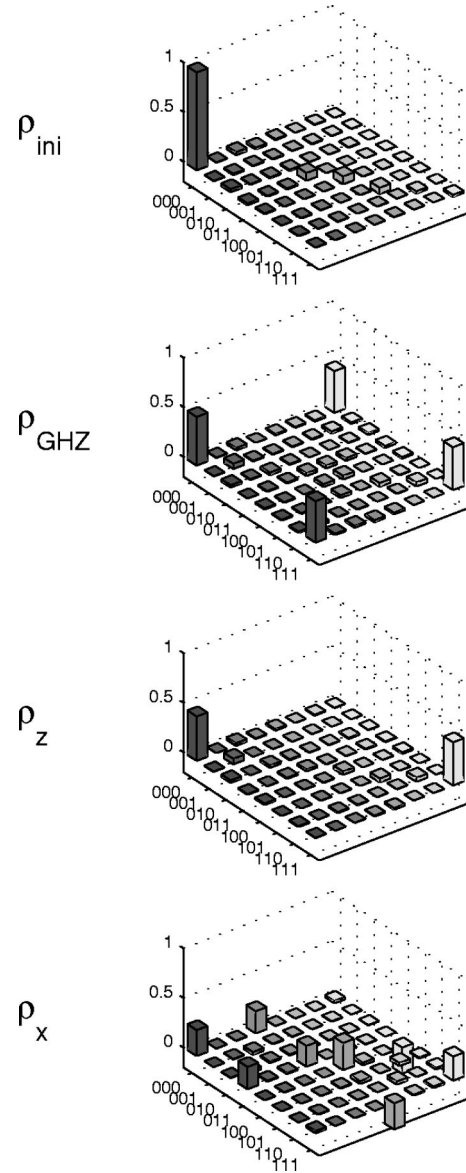


FIG. 6. Experimental density matrices reconstructed by tomography (in normalized units). The rows and columns are enumerated in the standard computational basis as described in Fig. 4. ρ_{ini} is the three-spin pseudopure ground state, and ρ_{GHZ} is the pseudopure GHZ state. The last two plots are ρ_z , which is ρ_{GHZ} after decohering spin 1 about the z axis, and ρ_x , which is after decohering it about the x axis. (Note: ρ_{GHZ} , ρ_z , and ρ_x have been magnified by a factor of 2 for clarity). An amount of identity, chosen to optimize the input projection, was added to all experimentally measured density matrices.

attenuated correlation of 0.93, showing that spins 2 and 3 were entangled before the GHZ state was created. The tomographic errors are estimated at $\pm 3\%$. As Fig. 6 shows, there is no entanglement present in ρ_z whereas in ρ_x the two-spin entanglement is recovered in the two subensembles of the ancilla spin following the σ_x^1 measurement.

Notice that if the result of the x -measurement were lost (i.e., the measured particle is traced over), the resulting reduced density matrix is maximally mixed. The state of the ancilla spin distinguishes these subensembles through its

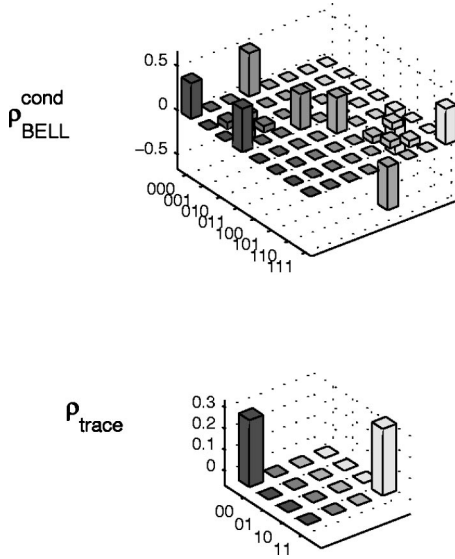


FIG. 7. The reconstructed conditional Bell and traced density matrices (in normalized units). The diagonal components have been shifted so unit trace is preserved. The top plot is the conditional Bell state (conditioned on the state of the ancilla qubit), while the bottom plot is the traced density matrix after applying the decoupling pulses to the ancilla qubit during the observation period.

coupling to the other two spins. Thus, we performed an experiment where the ancilla spin is directly decoupled by the NMR decoupling techniques discussed in Sec. IV. The result is shown in Fig. 7. This emphasizes the need of the measurement result to distinguish the two subensembles and retain quantum information.

2. The \bar{W} state

The W state preparation pulse sequence was based on a similar sequence used in a concurrently running experiment by our group [29]. This sequence acted as a NOT gate for the W state, $|\bar{W}\rangle$, which is equivalent to the W state if logical 1 is the ground state:

$$|\bar{W}\rangle \equiv \sigma_x^1 \sigma_x^2 \sigma_x^3 |W\rangle = \frac{1}{\sqrt{3}} (|110\rangle + |101\rangle + |011\rangle). \quad (45)$$

The logic network in Fig. 8 describes these experiments. The starting state is a three-spin pseudopure state, $\hat{\rho}_{\text{ini}}$, and the set of gates shown creates the pseudopure \bar{W} state:

$$\hat{\rho}_{\bar{W}} = \frac{1}{3} \left\{ \frac{1}{8} I + \frac{1}{2} \sigma_z^1 \sigma_z^2 \sigma_z^3 - E_+^1 E_+^2 E_+^3 + \frac{1}{2} [E_-^1 (\sigma_x^2 \sigma_x^3 + \sigma_y^2 \sigma_y^3) + E_-^2 (\sigma_x^1 \sigma_x^3 + \sigma_y^1 \sigma_y^3) + E_-^3 (\sigma_x^1 \sigma_x^2 + \sigma_y^1 \sigma_y^2)] \right\}. \quad (46)$$

While this expression highlights the symmetry of the state under particle exchange, the results are better explained by casting $\hat{\rho}_{\bar{W}}$ in terms of the states of spin 1 as follows:

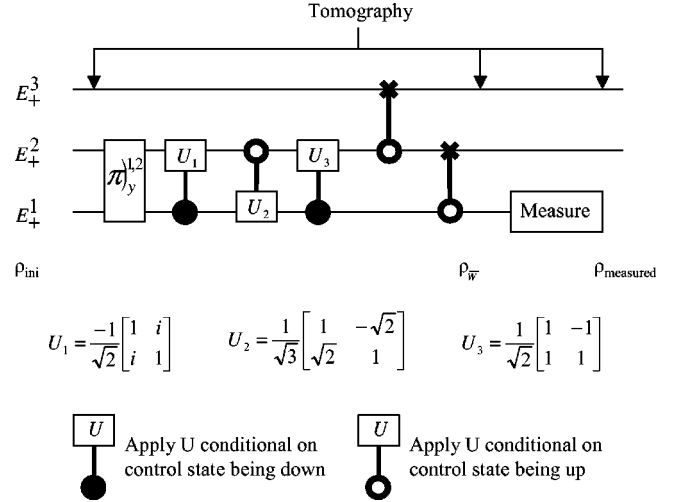


FIG. 8. Logic network for the creation of \bar{W} state followed by complementary measurements. Starting with ρ_{ini} the sequence of transformations shown creates $\rho_{\bar{W}}$. Subsequently, the set of complementary measurements described in the text are applied to spin 1 in the state $\rho_{\bar{W}}$.

$$\hat{\rho}_{\bar{W}} = \frac{\sqrt{3}}{4\sqrt{2}} \left\{ \frac{1}{3} [E_+^1 (E_-^2 E_-^3) + E_-^1 (1 + \sigma_x^2 \sigma_x^3) (E_+^2 E_-^3 + E_-^2 E_+^3) + \sigma_x^1 E_+^1 (\sigma_x^2 E_-^2 E_-^3 + E_-^2 \sigma_x^3 E_-^3) + \sigma_x^1 E_-^1 (\sigma_x^2 E_+^2 E_-^3 + E_-^2 \sigma_x^3 E_+^3)] - \frac{1}{8} I \right\}. \quad (47)$$

Note that the $|\tilde{\psi}_+\rangle$ state Eq. (12) has the GA representation $(1 + \sigma_x^2 \sigma_x^3) (E_+^2 E_-^3 + E_-^2 E_+^3)$, which here is multiplying the E_-^1 term. Subsequently, the same set of measurements from the disentanglement eraser P_z^1 and P_x^1 , Eqs. (41) and (42), respectively, are applied to $\hat{\rho}_{\bar{W}}$. The Appendix shows the GA representation of these states. While the P_z^1 measurement realizes the ensemble in Eq. (12), the P_x^1 measurement realizes the ensemble in Eq. (14). Tomographic readouts of these states, performed at the points indicated in Fig. 8, yield the reconstructed density matrices shown in Fig. 9. Once again only the real parts are shown because the imaginary parts were effectively zero.

The values of the attenuated correlation for each of the four tomographic readouts were $c(\hat{\rho}_{\text{ini}}^{\text{expt}}) = 1$ (by definition), $c(\hat{\rho}_{\bar{W}}^{\text{expt}}) = 0.77$, $c(\hat{\rho}_z^{\text{expt}}) = 0.80$ and $c(\hat{\rho}_x^{\text{expt}}) = 0.73$. As Fig. 9 shows both $\hat{\rho}_z^{\text{expt}}$ and $\hat{\rho}_x^{\text{expt}}$ retain the entangled state $(1 + \sigma_x^2 \sigma_x^3) (E_+^2 E_-^3 + E_-^2 E_+^3)$ in a subensemble; this is in contrast to the results for the complementary measurements of the GHZ state.

VI. CONCLUSIONS

In conclusion, we have used both a two-spin and a three-spin liquid-state NMR quantum information processor to obtain a high-precision implementation of the dynamics, both coherent and decoherent, underlying the quantum-eraser

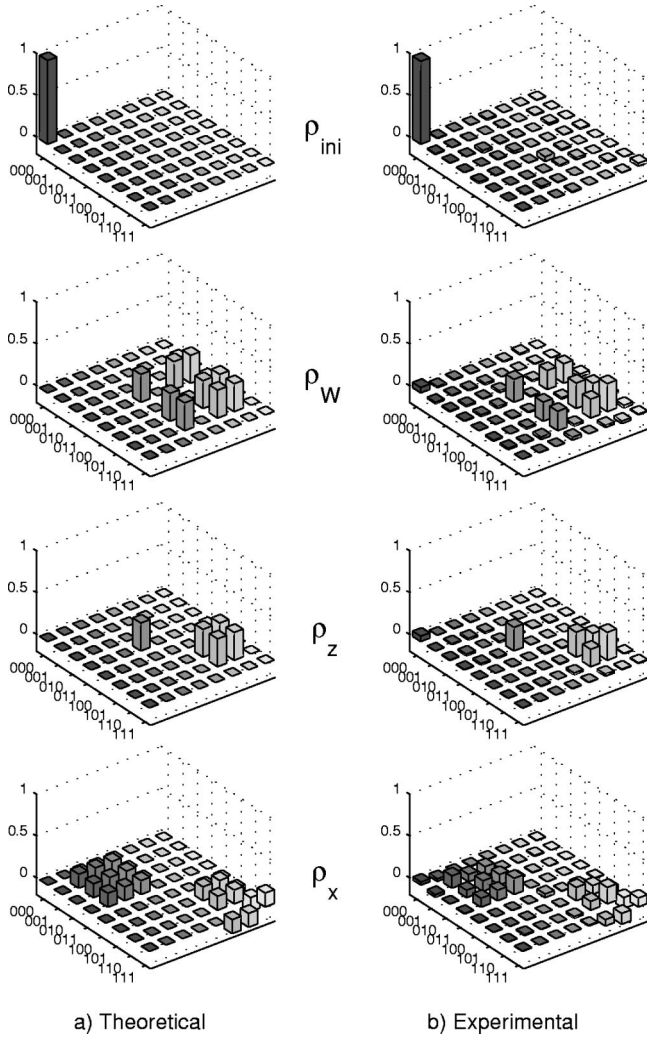


FIG. 9. Theoretical density matrices in (a) and experimental density matrices in (b) reconstructed by tomography (in normalized units). The rows and columns are enumerated in the standard computational basis as described in Fig. 4. In (b) ρ_{ini} is the three-spin pseudopure ground state, and $\rho_{\bar{W}}$ is the pseudopure \bar{W} state. The last two plots are ρ_z , which is $\rho_{\bar{W}}$ after decohering spin 1 about the z axis, and ρ_x , which is after decohering it about the x axis. An amount of identity, chosen to optimize the input projection, was added to all experimentally measured density matrices. The plots in (a) are the corresponding theoretical density matrices for comparison purposes.

scheme as applied to a Bell, GHZ and \bar{W} state followed by complementary measurements. We have found that the experimental results confirm the theoretically predicted conditional expectation values. Our study of the two-spin quantum eraser suggests that it may be used to transfer information shared amongst qubits based only on local decoherent operations assisted by classical communication. The three-spin results confirm the differences of the GHZ and \bar{W} state under the action of complementary local decoherent operations. A σ_z measurement of the ancilla spin yields separable states in the subensembles of the GHZ state while the same measurement in the \bar{W} state yields an entangled state in each sub-

semble. By contrast, a σ_x measurement of the ancilla spin in the GHZ state results in a maximally entangled state in both subensembles while the same measurements in the \bar{W} state result in mixtures of entangled and separable states in both subensembles.

A key feature of these experiments is the use of nonunitary control methods. Using gradient techniques we were able to judiciously and selectively render phase information macroscopically inaccessible in a way that precisely mimics the decoherence attendant on strong measurements. During this dephasing operation all interactions among the spins were refocused, and that only the *macroscopically accessible* information contained in the ancilla spin due to its earlier interactions with the other spins was changed.

With NMR decoupling methods we were able to perform a partial trace operation. By decoupling the ancilla spin, after the x measurement on the GHZ state the reduced density matrix yields a maximally mixed state. This further emphasizes the need for the ancilla spin to distinguish the subensembles after the measurement. Unlike previous eraser implementations, it was not necessary to explicitly read out this information in each member of the ensemble in order to see the conditional coherence, because this was done for us by the coupling of the ancilla to the other spins while the spectra were being measured.

ACKNOWLEDGMENTS

We thank L. Viola and S. Somaroo for helpful discussions. This work was supported by the U.S. Army Research Office under Grant No. DAAD 19-01-1-0519 and Grant No. DAAD 19-01-1-0678 from the Defense Advanced Research Projects Agency.

APPENDIX

The measurements P_z^1 and P_x^1 Eqs. (41) and (42), respectively, applied to $\hat{\rho}_{\bar{W}}$ in GA notation:

$$\hat{\rho}_{\bar{W}} \xrightarrow{P_z^1} \frac{\sqrt{3}}{4\sqrt{2}} \left\{ \frac{1}{3} [E_+^1 (E_-^2 E_-^3) + E_-^1 (1 + \sigma_x^2 \sigma_x^3) (E_+^2 E_-^3 + E_-^2 E_+^3)] - \frac{1}{8} I \right\}, \quad (\text{A1})$$

$$\begin{aligned} \hat{\rho}_{\bar{W}} \xrightarrow{P_x^1} & \frac{\sqrt{3}}{4\sqrt{2}} \left(\frac{1}{3} \left\{ \frac{1}{2} E_+^1 [E_-^2 E_-^3 + (1 + \sigma_x^2 \sigma_x^3) (E_+^2 E_-^3 + E_-^2 E_+^3)] \right. \right. \\ & + (\sigma_x^2 E_-^2 E_-^3 + E_-^2 \sigma_x^3 E_-^3) + (\sigma_x^2 E_+^2 E_-^3 + E_-^2 \sigma_x^3 E_+^3) \\ & + \frac{1}{2} E_-^1 [E_-^2 E_-^3 + (1 + \sigma_x^2 \sigma_x^3) (E_+^2 E_-^3 + E_-^2 E_+^3)] \\ & - (\sigma_x^2 E_-^2 E_-^3 + E_-^2 \sigma_x^3 E_-^3) \\ & \left. \left. - (\sigma_x^2 E_+^2 E_-^3 + E_-^2 \sigma_x^3 E_+^3) \right\} - \frac{1}{8} I \right). \end{aligned} \quad (\text{A2})$$

- [1] M. O. Scully and K. Druhl, Phys. Rev. A **25**, 2208 (1982); M. O. Scully, B. G. Englert, and H. Walther, Nature (London) **351**, 111 (1991); M. O. Scully and M. S. Zubairy, *Quantum Optics* (Cambridge University, Cambridge, England, 1997).
- [2] R. Garisto and L. Hardy, Phys. Rev. A **60**, 827 (1999).
- [3] G. Teklemariam, E. M. Fortunato, M. A. Pravia, T. F. Havel, and D. G. Cory, Phys. Rev. Lett. **86**, 5845 (2001).
- [4] W. Dür, G. Vidal, and J. I. Cirac, Phys. Rev. A **62**, 062314 (2000).
- [5] F. Verstraete, J. Dehaene, B. De Moor, and H. Verschelde, e-print quant-ph/0109033.
- [6] K. M. O'Connor and W. K. Wotters, Phys. Rev. A **63**, 052302 (2001).
- [7] A. Wong and N. Christensen, Phys. Rev. A **63**, 044301 (2001).
- [8] J. Eisert and H. J. Briegel, Phys. Rev. A **64**, 022306 (2001).
- [9] G. Vidal and R. F. Werner, e-print quant-ph/0102117.
- [10] D. A. Meyer and N. R. Wallach, e-print quant-ph/0108104.
- [11] E. T. Jaynes, *Foundations of Radiation Theory and Quantum Electrodynamics*, edited by A. O. Barut (Plenum, New York, 1980).
- [12] P. G. Kwiat, A. M. Steinberg, and R. Y. Chiao, Phys. Rev. A **49**, 61 (1994); T. J. Herzog, P. G. Kwiat, H. Weinfurter, and A. Zeilinger, Phys. Rev. Lett. **75**, 3034 (1995); P. G. Kwiat, P. D. D. Schwindt, and B.-G. Englert, *Mysteries, Puzzles and Paradoxes in Quantum Mechanics*, edited by R. Bonifacio (AIP, New York, 1999).
- [13] J. M. Raimond, M. Brune, and S. Haroche, Phys. Rev. Lett. **79**, 1964 (1997).
- [14] E. M. Fortunato, M. A. Pravia, N. Boulant, G. Teklemariam, T. F. Havel, and D. G. Cory, J. Chem. Phys. **116**, 7599 (2002).
- [15] T. F. Havel, Y. Sharf, L. Viola, and D. G. Cory, Phys. Lett. A **280**, 282 (2001).
- [16] D. G. Cory, R. Laflamme, E. Knill, L. Viola, T. F. Havel, N. Boulant, G. Boutis, E. Fortunato, S. Lloyd, R. Martinez, C. Negrevergne, M. Pravia, Y. Sharf, G. Teklemariam, Y. S. Weinstein, and W. H. Zurek, Fortsch. Phys. **48**, 875 (2000).
- [17] R. Freeman, *Spin Choreography* (Oxford University, Oxford, United Kingdom, 1998).
- [18] M. D. Price, T. F. Havel, and D. G. Cory, Physica D **120**, 82 (1998).
- [19] S. S. Somaroo, D. G. Cory, and T. F. Havel, Phys. Lett. A **240**, 1 (1998).
- [20] J. S. Waugh, J. Magn. Reson. (1969-1992) **50**, 30 (1982).
- [21] A. Sodickson and D. G. Cory, Prog. Nucl. Magn. Reson. Spectrosc. **33**, 77 (1998).
- [22] Y. Sharf, D. G. Cory, T. F. Havel, S. S. Somaroo, E. Knill, R. Laflamme, and W. H. Zurek, Mol. Phys. **98**, 1347 (2000).
- [23] J. A. Jones and E. Knill, J. Magn. Reson. **141**, 322 (1999).
- [24] M. A. Pravia, E. Fortunato, Y. Weinstein, M. D. Price, G. Teklemariam, R. J. Nelson, Y. Sharf, S. Somaroo, C. H. Tseng, T. F. Havel, and D. G. Cory, Concepts Magn. Reson. **11**, 225 (1999).
- [25] T. F. Havel, S. S. Somaroo, C. H. Tseng, and D. G. Cory, Appl. Alg. Eng. Comm. Comput. **10**, 339 (2000).
- [26] A. Steane, Rep. Prog. Phys. **61**, 117 (1998).
- [27] I. L. Chuang, L. M. K. Vandersypen, X. Zhou, D. W. Leung, and S. Lloyd, Nature (London) **393**, 143 (1998).
- [28] R. J. Nelson, D. G. Cory, and S. Lloyd, Phys. Rev. A **61**, 022106 (2000).
- [29] L. Viola, E. M. Fortunato, M. A. Pravia, E. Knill, R. Laflamme, and D. G. Cory, Science **293**, 2059 (2001).